Journal of ELECTRONIC MATERIALS
DOI: 10.1007/s11664-015-4137-2

Control of Phase in Tin Sulfide Thin Films Produced via RF-Sputtering of SnS_2 Target with Post-deposition Annealing

R.E. BANAI,[1,3] J.C. CORDELL,[1] G. LINDWALL,[1] N.J. TANEN,[2] S.-L. SHANG,[1] J.R. NASR,[2] Z.-K. LIU,[1] J.R.S. BROWNSON,[1] and M.W. HORN[1,2]

1.—Materials Science and Engineering Department, The Pennsylvania State University, University Park, Pennsylvania 16802, USA. 2.—Engineering Science and Mechanics Department, The Pennsylvania State University, University Park, Pennsylvania 16802, USA. 3.—e-mail: rona.banai@gmail.com

Tin (II) Monosulfide (SnS) has become an interesting new material for thin film photovoltaics. SnS-based devices have achieved limited success in improved solar cell efficiency. While annealing is a typical post-deposition treatment used to improve thin film quality, sulfur volatility is an issue, despite strong Sn-S bonds in tin sulfide compounds. Annealing of sulfur-rich sputtered tin sulfide thin films in a vacuum environment has not been previously reported. In the present work, we investigated the optoelectronic properties, crystallographic phase, and morphology of annealed, sputtered tin sulfide thin films. Specifically, we studied the phase change and improvement in material quality as a result of post-deposition heat treatments. Tin sulfide thin films were sputtered with and without substrate heating. These samples were then annealed between 300°C and 500°C under moderate vacuum ($<1 \times 10^{-4}$ Pa) in the deposition chamber to find the optimal annealing process for producing α-SnS. Significantly improved crystallinity and morphology were seen in sulfur-rich thin films annealed at 400–500°C for 60 min. Annealed films had resistivity in the range of 30–300 Ω-cm. Experimental observations were confirmed by calculated phase diagrams, which show that annealing around 400°C at low pressure is optimal to obtain a phase-pure α-SnS film from an amorphous SnS_2 film.

Key words: Tin chalcogenides, SnS, sputtering, thin films, optoelectronic properties, phase diagram

INTRODUCTION

Tin (II) monosulfide (SnS) is considered a promising new absorber material for next-generation thin-film photovoltaic (PV) technology. SnS has a bandgap energy of ~1.1–1.3 eV,[1,2] a large above-bandgap optical absorption coefficient of 10^4–10^5 cm^{-1},[3] a high native free-carrier concentration of ~10^{15} cm^{-3},[4] and an earth abundance of its constituent elements. Despite these properties, which suggest that PV devices with efficiencies as high as 24% are possible based on Loferski's analysis of similar materials,[5] efficiencies of SnS-based devices are lower than 5%,[6] with most results near or below 1% efficiency.[4,7,8] In order to improve the efficiency of SnS solar cells, different approaches have been tried. Crystalline quality has been improved,[9] optimum device architecture has been suggested,[1] and detrimental effects of the secondary phases, such as SnS_2 and Sn_2S_3, potentially present in SnS layer on the device performance, have been examined.[10]

Many different methods have been utilized to produce SnS thin films, including spray pyrolysis,[4,11] thermal evaporation,[3,12,13] atomic layer deposition,[9] sputtering of SnS target,[14,15] and electrochemical deposition.[16] One shortfall of thermal-based methods is the challenge to maintain a 1:1

(Received May 6, 2015; accepted October 5, 2015)

Published online: 19 October 2015

ratio of Sn:S. The high volatility of sulfur requires excess sulfur in the system to ensure the deposition of stoichiometric material. The challenge to maintain stoichiometric SnS extends further for post-deposition heat treatments. Slight tin deficiency is preferable, as tin vacancies will yield *p*-type material. According to calculations for single crystal α-SnS, Burton et al.[10] found that 10^{19} cm^{-3} tin vacancies form, while only 10^{12} cm^{-3} sulfur vacancies form. Tin vacancies form easily due to their low formation energy. The high concentration of tin vacancies relative to sulfur vacancies will cause SnS to be *p*-type.[10]

While these calculations are for single crystal α-SnS, they can be used as a model for thin film material. The literature shows that films have a tendency to be sulfur deficient,[3,12,15] with potential for tin migration to grain boundaries, surfaces, interfaces, interstitial sites, or sulfur anti-sites. All of these can be related to poor device performance. Even with these defects, sulfur-deficient films are still usually *p*-type due to the high concentration of tin vacancies.[3,12,15]

Sputter deposition is a process that can easily be scaled for production. Films made from a SnS target have been previously reported, but the results have been less than ideal.[14,17,18] Sousa et al. reported results on the annealing of films sputtered from a SnS_2 target deposited at room temperature.[19] Their methods focused on furnace annealing in sulfur environment with a N_2 + 5% H_2 as the carrier gas. In their study, films were also annealed in the inert environment without sulfur. They found that an annealing temperature of 570°C for 15 min in a N_2 + 5% H_2 500 mbar overpressure was sufficient to form a uniform SnS phase, and that no sulfur partial pressure was the best for producing an phase-pure α-SnS film. Despite a uniform SnS phase, the indirect band gap was found to be 1.37 eV, which is higher than the expected 1.1 eV.[2,8] The direct band gap of 1.41 eV was closer to the expected value of 1.3–1.5 eV.[2,7]

Understanding the phase relationship as a function of pressure, temperature, and composition is important for developing the best process for SnS thin films. Tin and sulfur are both volatile, but sulfur tends to volatilize more easily than tin. For the past few decades, a Sn-S phase diagram at atmospheric pressure has been the only available reference.[20] We have modeled the Sn-S system using the CALPHAD (CALculation of PHase Diagrams) method,[21,22] aided by first-principles calculations.[23] The approach makes it possible to calculate thermodynamic properties as a function of composition, pressure and temperature, and hence, provide quantitative phase stability to guide the experiment design and to increase the understanding of experimental outcomes similar to the thin film growth of MgB_2 and $BiFeO_3$.[24,25]

Sputtering from a SnS_2 target produces sulfur-rich tin sulfide thin films, which can be annealed to form various tin sulfide phases, depending on annealing temperature and time. The goal of this work was to pursue an alternative avenue for producing highly crystalline α-SnS thin films that are not sulfur deficient. Two heater types were employed to anneal films at moderate vacuum: (1) a resistive rod heater and (2) a halogen bulb as the heating elements. The major difference between these heater types was their thermal mass, affecting ramp and cool down times. The effects of annealing temperature and time were also studied. Phase diagrams were calculated to provide a thermodynamic perspective when interpreting the annealing results. The impact of annealing on films with and without *in situ* heating was also evaluated.

EXPERIMENTAL

Tin sulfide thin films were deposited in a radio frequency (RF) magnetron sputtering system in a downward vertical geometry at room temperature. Films were deposited using a 3″ diameter tin disulfide (SnS_2) target of 99.999% purity (LTS Research Laboratories, Inc.). Films were co-deposited on silicon-nitride–coated silicon wafers and glass microscope slides. Target-to-substrate throw distance was 11 cm. A turbomolecular pump allows the chamber to reach base pressures below 2.66×10^{-5} Pa. Samples were deposited at 1.33 Pa for 10 min with plasma power of 115 W. Most samples were deposited with no substrate heating (RT), but some samples had substrates heated to 150°C. Samples were annealed for 30 min or 60 min between 300°C and 500°C. As-deposited samples were also studied for comparison to annealed samples.[14,17]

Annealing in moderate vacuum ($<10^{-4}$ Pa) was done in the same chamber as the deposition. Annealing immediately after deposition without breaking vacuum helped minimize any surface oxides that could form prior to annealing. Two types of heaters were used for post-deposition annealing to develop an optimal and repeatable process for producing α-SnS. The first was a resistive heater with a large thermal mass, while the second was a halogen lamp to heat a thin copper stage. The ramp time and cool down time was much longer for the resistor heater than for the halogen heater. Ramp times for the resistive and halogen heaters were about 15 min and 8 min, respectively, while cool down times were 4 h and 2 h, respectively, for a 400°C anneal. Sample C4 had two levels of heating. The heater temperature was quickly increased to 350°C in <5 min, which was followed by a slow increase to 400°C in about 30 min. A 60-min annealing time was measured from the time it reached 400°C. Ramp time and cool down time impacted film properties; therefore, annealing time was adjusted to replicate results. Table I summarizes deposition conditions of the samples examined in this study. The prefix in the sample name was designated to key process conditions: “A” for non-annealed samples, “C” for samples annealed in vacuum with the

Table I. Summary of samples deposition conditions and annealing specifications

Sample name	Average substrate temperature (°C)	Heater	Annealing temperature (°C)	Annealing time (min)	Thickness (nm)
A1	38	N/A	–	–	310
A2	150	N/A	–	–	380
C1	38	Halogen	400	30	340
C2	38	Halogen	400	60	280
C3	38	Halogen	500	60	250
C4	38	Halogen	400	60	276
D1	38	Resistive	300	30	230
D2	150	Resistive	300	30	370
D3	38	Resistive	400	30	220
D4	150	Resistive	400	30	300

halogen heater, and "D" for samples annealed in vacuum with the resistive heater.

Film thickness was determined using a Tencor profilometer. Surface morphology of the films was assessed using a Zeiss SMT 1530, high-resolution field emission scanning electron microscope (FESEM). Composition was determined via electron dispersive spectroscopy (EDS) using an FEI Nova NanoSEM 630 FESEM with an EDAX detector. A single crystal sample of SnS was used as a standard for this measurement. Phase analysis was determined from x-ray diffraction (XRD) patterns. XRD measurements of films were done on a PANalytical X'Pert PRO MPD in grazing incidence mode at an incident angle of 1° and detected from 10° to 70°.

When possible, band gap energies were determined for films using spectroscopic ellipsometry data. Films were measured using a Woollam dual rotating compensator spectroscopic ellipsometer (RC2). Data were analyzed in CompleteEASE to determine the complex index of refraction, using a general oscillator to model the optical constants. The imaginary component, or extinction coefficient (k) was used to determine the absorption coefficient (α) using the following equation:

$$\alpha = 4\pi k/\lambda \quad (1)$$

Tauc plots were used to extract band gap from the α. Further details regarding the analysis are described in previous work.[14]

Resistivity was determined using TLM measurements. Titanium (Ti) contacts were sputtered on the surface of samples using a stencil mask. The TLM pattern consisted of five lines 6-mm long, spaced 0.2 mm, 0.3 mm, 0.5 mm, and 0.7 mm apart. Films with low resistivity (<200 Ω-cm) values were also checked using a four-point probe. Conductivity type of thin films was extracted from hot probe measurements. In this technique, the voltage difference across two probes, one heated one at room temperature, was measured using a soldering iron as the heat source. The sign of the voltage drop detected indicates the carrier type.[26]

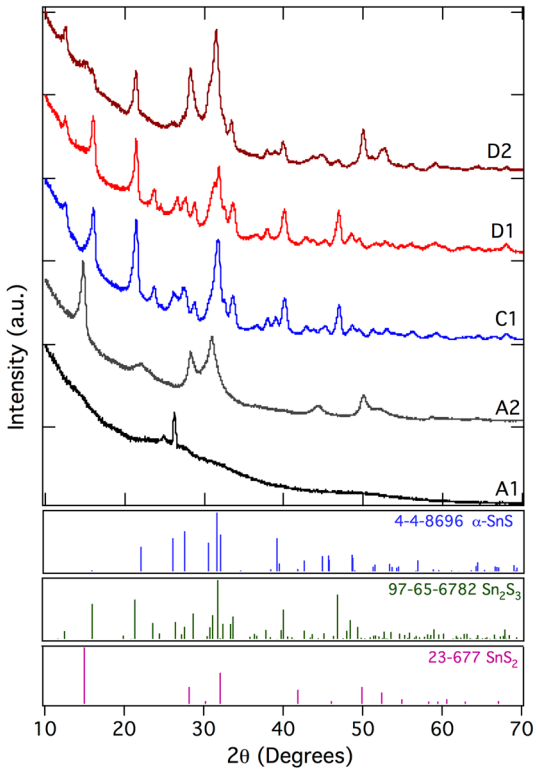

Fig. 1. XRD data for films where annealing resulted in films with Sn_2S_3 or SnS_2 as the primary phases.

CALCULATIONS

In CALPHAD modeling, one uses thermochemical data (measured or calculated from first-principles) and phase equilibrium data to evaluate model parameters for the Gibbs free energy of individual phases as a function of temperature, composition and pressure for each phase relevant for the system. Phase diagrams can then be calculated at any given conditions by minimizing the total Gibbs free energy of the system, and hence, thermodynamic information is not restricted only to those conditions for which experimental data is available. In the present

work, the software Thermo-Calc was used for all phase diagram calculations.

RESULTS

Experimental Results

Films characterized for these experiments were separated into two categories: (1) films that contain high-sulfur content phases and (2) films that are a phase-pure α-SnS. XRD patterns and SEM micrographs for films fitting the first category are shown in Figs. 1 and 2, respectively. Powder diffraction files (PDFs) that match the phases present in the films are shown in Fig. 1. Sample A1 is mainly amorphous, as were all films grown at room temperature with the SnS_2 target. Three unique PDFs can be used to match the phases in the other tin sulfide thin films: herzenbergite, or α-SnS (PDF #4-4-8696; *Ortho*; *Pbnm;* a = 4.329, b = 11.192, and c = 3.984 Å), berndtite SnS_2 (PDF #23-677; *Hexagonal*; *P-3m1;* $a = b$ = 3.65 and c = 5.90 Å), and ottemannite Sn_2S_3 (PDF #97-65-6782; *Ortho; Pmna;* a = *8.864,* b = 3.747, and c = 14.020 Å). As-deposited films grown with substrate heating or annealed films typically crystallized into at least one of these phases. Figure 1 shows XRD patterns for films with higher sulfide phases SnS_2 or Sn_2S_3. Some of these films also have α-SnS present. Sample A2, shown in Fig. 1, has some similar peaks matching SnS_2, suggesting its presence in these films. Samples C1, D1, and D2 primarily contain Sn_2S_3. Remnants of SnS_2 are evident for sample D2, which was annealed from a sample similar to sample A2. The result suggests that it is harder to convert the crystalline SnS_2 film to Sn_2S_3, whereas samples C1 and D1 were annealed from amorphous material that more easily formed a uniform Sn_2S_3 phase.

Figure 3 shows XRD patterns of films with the second category of films, with only α-SnS phase and morphology of these films shown in Fig. 4. These films were annealed at sufficiently high temperature for sufficient time to yield α-SnS; however, remnants of other tin sulfide phases may be present

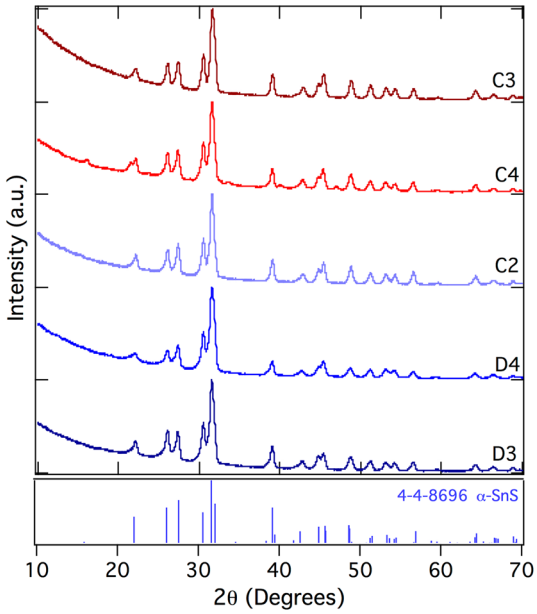

Fig. 3. XRD pattern for films in which resulted in a complete phase change to α-SnS.

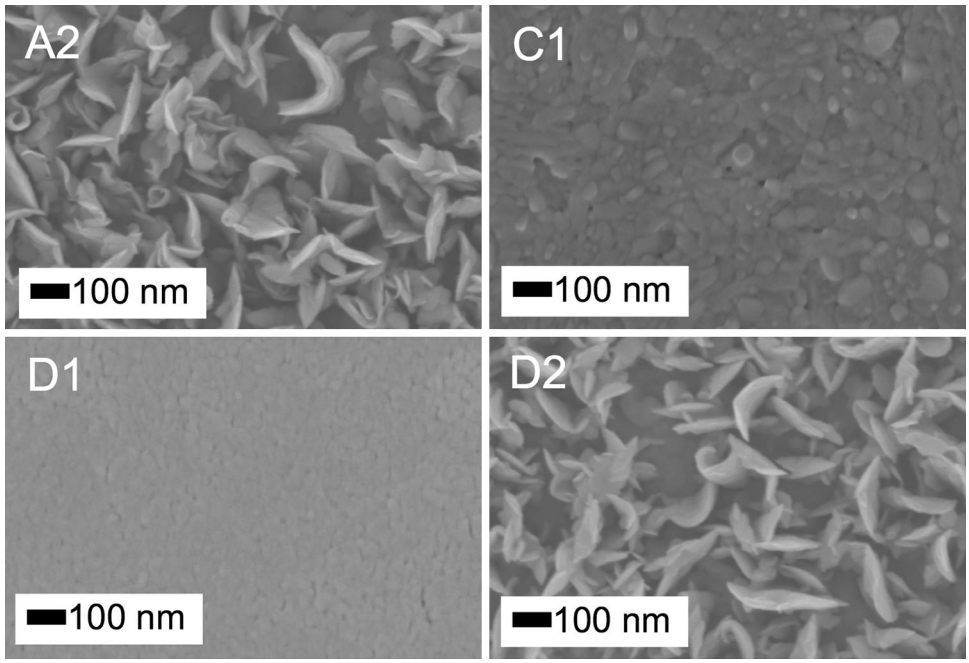

Fig. 2. SEM micrographs of films with multiple phases or high sulfur content phases (SnS_2 or Sn_2S_3).

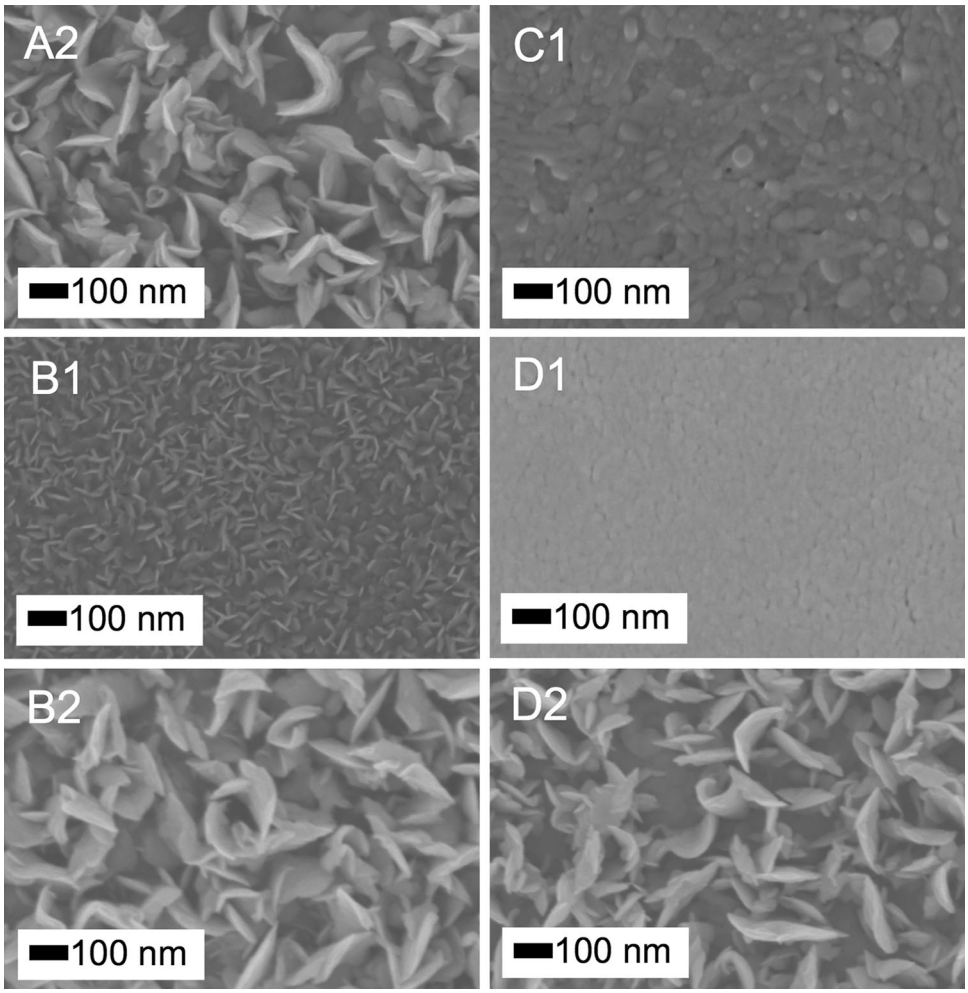

Fig. 4. SEM micrographs of samples exhibiting α-SnS phase.

Table II. Resistivity for films determined by TLM measurements with Ti top contacts and four-point probe

Sample name	Resistivity from TLM (Ω-cm)	Resistivity from 4 pp (Ω-cm)	Conductivity type	Direct band gap (eV)
C1	7.9×10^4	Out of range	Unknown	Unknown
C2	41	27 ± 4	*p*-Type	1.27 ± 0.03
C3	60	35 ± 4	*p*-Type	1.27 ± 0.02
C4	Not meas.	31 ± 8	*p*-Type	1.11 ± 0.03
D1	2.7×10^5	Out of range	*n*-Type	0.93 ± 0.03
D2	1.1×10^3	Out of range	*p*-Type	Unknown
D3	1.0×10^3	16 ± 2	*p*-Type	1.25 ± 0.02
D4	79	30 ± 4	*p*-Type	Unknown

in small quantities, not detectable by XRD. The PDF for α-SnS is also shown in Fig. 3, with peaks aligning well with this phase. Figure 4 shows both SEM micrographs of films grown on glass and silicon substrates for sample C4. Heater ramp time and cool time impacted film morphology significantly, and is seen in parallel for different substrates, as glass and silicon have different thermal conductivity values.

Each phase has a different density, resulting in variation in film thickness, shown in Table I. Crystallite formation during the heated depositions also impacted film thickness. Sample A1, which was amorphous was much thinner than crystalline

sample A2. This impacted the final thicknesses of samples from the "D" series, which were annealed from samples produced identically to samples A1 and A2. The total change in thickness was about equal for all of these films, but the final thickness was dependent on the starting thickness.

Band gaps of some films were determined from spectroscopic ellipsometry data, and are listed in Table II. Films with α-SnS as the dominant phase all have band gaps in the range of 1.1–1.3 eV. For some films, an optical model with low error values could not be determined, and a band gap could not be extracted for those films. Large error values were likely caused by an inability to model a highly irregular thin film, and suggests that the films were non-uniform.

TLM measurements of films from the "C" and "D" series showed that films deposited with *in situ* heating have resistivity values several orders of magnitude lower than those deposited at room temperature and subsequently annealed (Table II). Resistivity of samples was also checked using a four-point probe. Only samples exhibiting a dominant α-SnS phase could be measured. Other samples had resistivity too large for our measurement system. Films grown on both silicon and glass substrates were measured by four-point probe. Figure 5 shows the resistivity measured by four-point probe and TLM with top Ti contacts versus base pressure of the chamber prior to deposition. Measurements from the four-point probe show that for the glass substrates, there is a slight trend of improved resistivity for lower base pressure. This may be due to less oxygen or nitrogen impurities in the film. However, this trend is not seen for TLM measurements. All samples made on both substrates were measured; however, some films on oxidized silicon had a resistivity that was too high for four-point probe measurements. There is insufficient data to suggest a trend for the resistivity determined by TLM, although they follow a similar trend for films from the same deposition run, as indicated by the grey arrows. No trend was observed for films based on annealing temperature or time.

Conductivity type of films is listed in Table II. Sample D1 is *n*-type, while all others measured are *p*-type. According to its XRD pattern, sample D1 is Sn_2S_3, which can be either *p*-type or *n*-type, depending on the dominant vacancy. This film likely has more sulfur vacancies than tin vacancies, causing it to be *n*-type. All α-SnS films were found to be *p*-type, which is likely the result of tin vacancies forming. Films without known conductivity likely do not have a dominant carrier type, due to compensating defects.

Phase Diagram Calculations

The conditions selected for the present phase diagram calculations included pressure-composition (*P*-*x*) diagrams at the annealing temperatures of 300°C, 400°C and 500°C (Fig. 6) and a temperature-composition (*T*-*x*) diagram at 2.67×10^{-5} Pa and 1.33×10^{-4} Pa (Fig. 7), which are within the expected range of pressure established for annealing. In addition, a phase diagram was calculated showing the sulfur partial pressure as a function of temperature (Fig. 8). This diagram was used to investigate how the phase equilibria changed if the sulfur partial pressure of the annealing atmosphere varied.

The conversion of the deposited S-rich films to α-SnS during the annealing is a kinetic process, and consequently, the course of events cannot solely be predicted by thermodynamics. However, thermodynamic information can provide valuable insight and guidance when selecting process parameters, so that the α-SnS is the stable solid phase in equilibrium with the gas phase.

The initial S-rich film is a metastable structure and transformation to an equilibrium phase occurs during annealing. From a thermodynamic point of view, a number of different outcomes are possible, depending on annealing temperature and pressure. To demonstrate this, three pressure-composition phase diagrams are calculated at three different temperatures, 300°C, 400°C and 500°C (Fig. 6). The ranges of base pressure (1.33×10^{-5}–1.33×10^{-4} Pa) that are expected in the annealing chamber for annealing of C and D samples are marked in grey in the figures.

At 300°C, Fig. 6a, formation of pure α-SnS films cannot be expected, as the equilibrium phases for

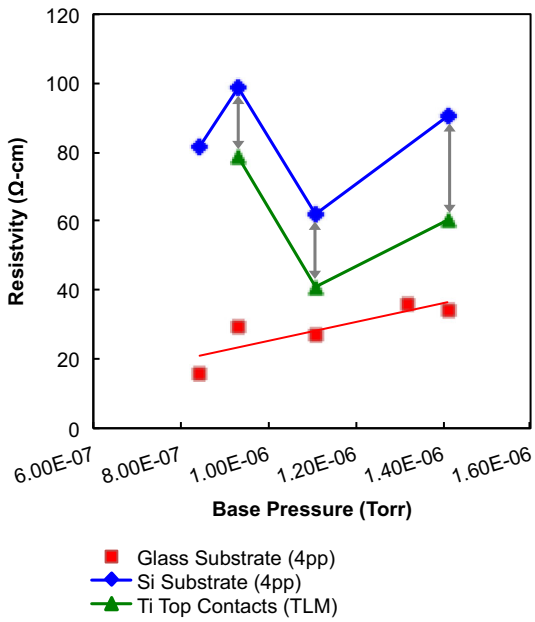

Fig. 5. Resistivity measurements determined from four-point probe measurements and TLM with Ti top contacts for samples exhibiting α-SnS phase versus base pressure of the chamber prior to deposition.

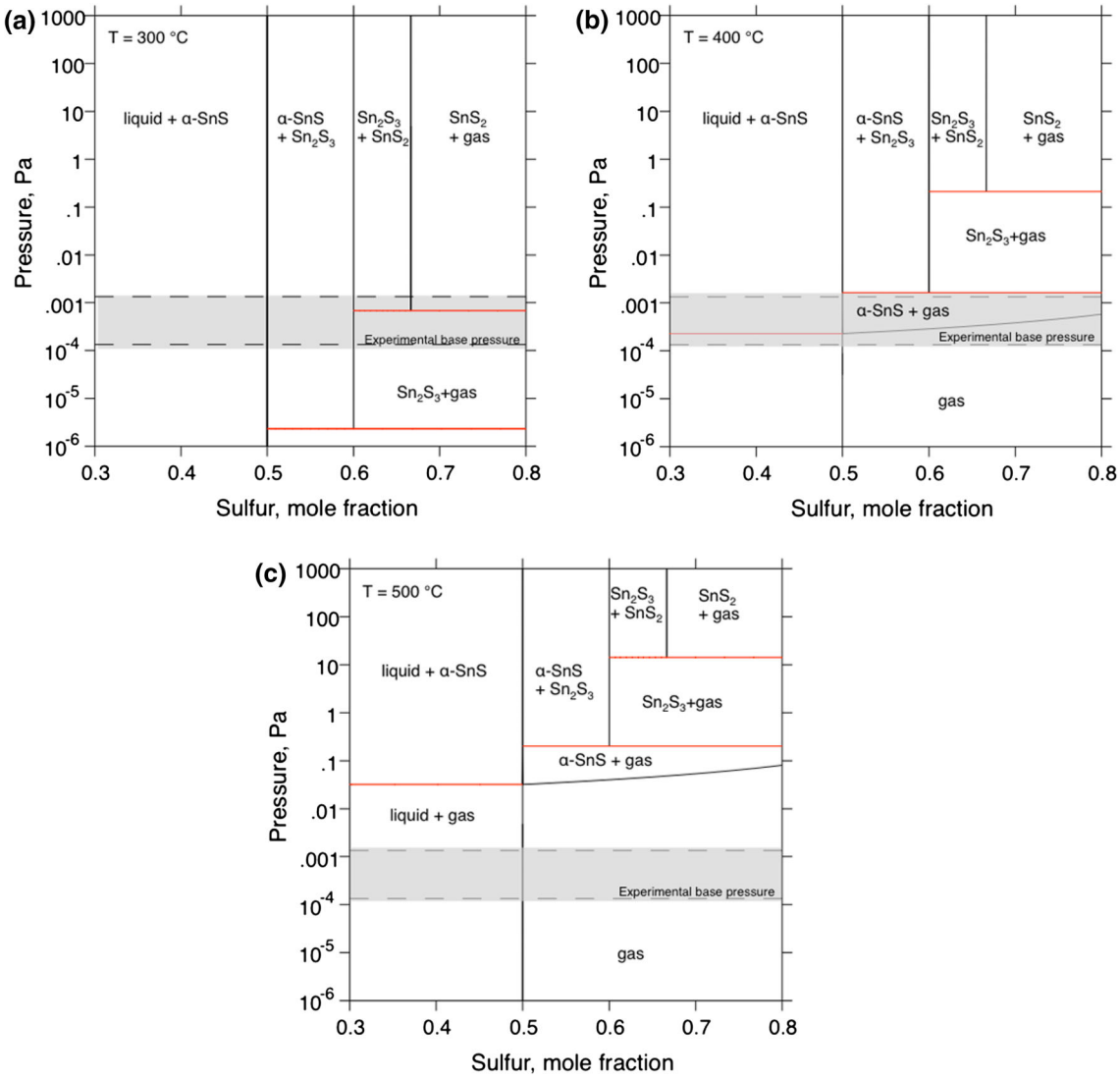

Fig. 6. Calculated pressure-composition phase diagrams at (a) 300°C, (b) 400°C, and (c) 500°C. The experimental base pressure, 10^{-6}–10^{-5} Torr (1.33×10^{-5}–1.33×10^{-4} Pa), is marked to indicate the stability regions in the pressure range.

the concerned pressure range is either (1.33×10^{-5}–1.33×10^{-4} Pa) "Sn_2S_3 + gas" or "α-SnS + Sn_2S_3" depending on the excess amount of sulfur. In Fig. 6b, the phase diagram at 400°C is shown. At this temperature, the base pressure range in the annealing chamber contains the "α-SnS + gas" stability region, and successful annealing results are to be expected, as long as the annealing time is not too short. The phase diagram in Fig. 6c tells us that at 500°C, the only stable phase is gas for all sulfur contents at and above 50%.

In Fig. 7a and b, temperature-composition phase diagrams are shown for 2.67×10^{-5}–1.33×10^{-4} Pa, respectively. This diagram suggests that an annealing temperature between 370°C and 400°C or 395°C and 430°C, respectively, should be selected to ensure that a phase-pure α-SnS film is the result. Preferably, a temperature from the higher portion of the temperature interval should be selected to shorten the required annealing time.

DISCUSSION

Characteristics for as-deposited films were determined prior to annealing. Films grown with no substrate heating during the deposition had no peaks or minimally identifiable peaks prior to annealing, suggesting minimal crystallization, as seen for sample A1 in Fig. 1. The broad hump is consistent with the XRD pattern seen for a clean glass substrate and typical of amorphous materials, also seen by Sousa et al.[19] All non-annealed films showed barely detectable nanocrystalline morphology from SEM micrographs. These films exhibited high contact resistances on the order of 10 MΩ with Ti top contacts. Thin film resistivity was not

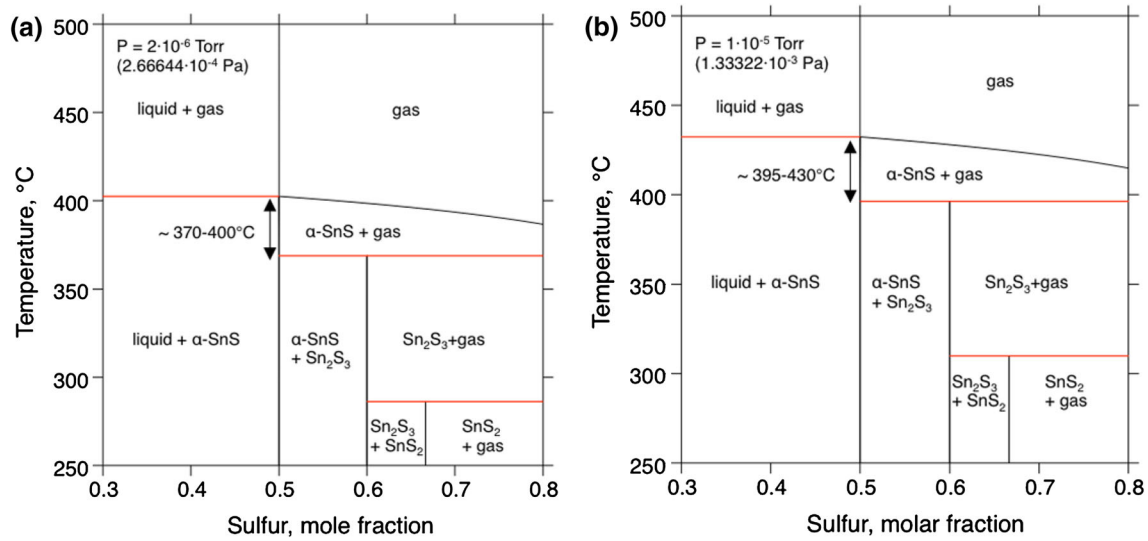

Fig. 7. Calculated temperature-composition phase diagrams at (a) 2×10^{-6} Torr (2.67×10^{-4} Pa) and (b) 1×10^{-5} Torr (1.33×10^{-4} Pa). The temperature range at compositions close to 50% sulfur for which α-SnS is expected to be stable together with gas is marked.

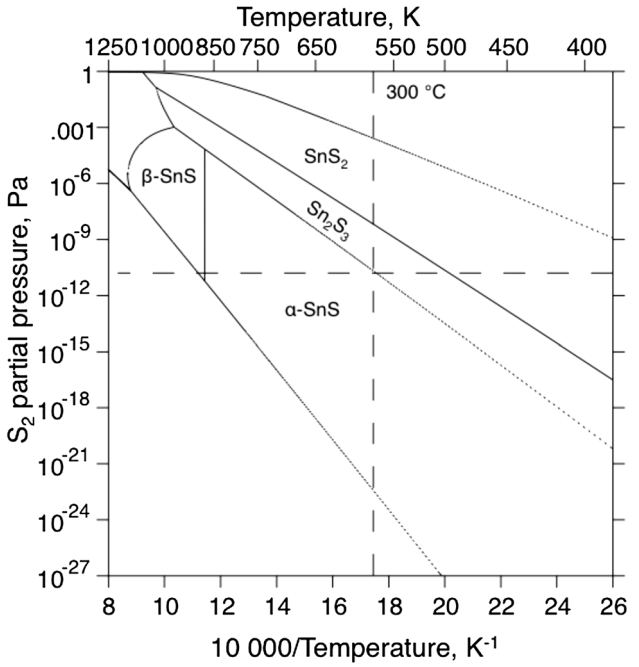

Fig. 8. Calculated S_2 partial pressure–temperature phase diagrams at 100 kPa. The temperature 300°C is marked to show the lowest S_2 partial pressure that is possible if the S-richer phases Sn_2S_3 and SnS_2 phases should be avoided.

detectable by TLM due to the high contact resistance, and the resistivity was too high to measure using the four-point probe.

Films deposited with substrate heating crystallized at 150°C. Sample A2 is an example of this result, with its XRD pattern shown in Fig. 1, matching the SnS_2 phase. The film morphology matches of sample A2 is shown in Fig. 2. Resistivity of films deposited around 150°C were typically <100 Ω-cm, as determined from Ti TLM top contacts. The stark difference in crystallinity of these films was used to determine the impact of post-deposition film processing.

During annealing, several reactions can occur that affect the final crystal structure. Reactions 1–4 listed below represent the transformation of SnS_2 as it is annealed.[19,27] Control of these reactions is important for guaranteeing the formation of a uniform phase. Reaction 4 is a dissociation reaction predicted by Sousa et al.[19]

$$SnS_2(s) \rightarrow \tfrac{1}{2}Sn_2S_3(s) + \tfrac{1}{4}S_2(g) \quad (1)$$

$$Sn_2S_3(s) \rightarrow 2SnS(s) + \tfrac{1}{2}S_2(g) \quad (2)$$

$$SnS(s) \rightarrow SnS(g) \quad (3)$$

$$Sn_2S_3(s) + SnS_2(s) \rightarrow 3SnS(s) + 5S(g) \quad (4)$$

These reactions predict that the presence of sulfur gas will suppress the formation of single phase SnS as SnS_2 and Sn_2S_3 will form. Figure 8 shows that annealing in a sulfur environment to yield α-SnS must be done at very low sulfur vapor pressure (10^{-11} Pa). This small vapor pressure would be very challenging to achieve precisely, suggesting that no added sulfur pressure is best for annealing α-SnS.

Our experimental results match the calculated phase diagrams in that annealing for 1 h at 400°C produced α-SnS, while lower temperatures or shorter time at 400°C produced Sn_2S_3. As the system moves to lower pressure, a phase separation region of α-SnS and tin-sulfur gas develops. At 300°C, Sn_2S_3 is stable at the system pressures of the experimental work presented here, as shown in Fig. 6a. According to Fig. 6b and c, both 400°C and 500°C are reasonable temperatures for the forma-

tion of α-SnS, but system pressure is important. At 500°C, the system pressure used for our experiments was too low for optimal conversion to α-SnS. If the annealing was allowed to proceed for longer times, the whole film should have evaporated based on the phase diagram. At higher pressure, it is expected that the process will be less sensitive to the annealing time.

Annealing of amorphous films differed in morphology and XRD patterns compared to annealing crystalline films. Recrystallization requires much more energy than producing a crystalline phase from an amorphous film. This is seen in the morphology shown in Figs. 2 and 4, where films grown at 150°C do not show significant change after annealing. Conversion of the film to α-SnS from a crystalline film was possible at 400°C with the resistive heater, but its morphology shows remnants of the original film. Annealing amorphous films at 400°C consistently formed α-SnS, using the halogen heater.

α-SnS formed for films annealed at temperatures above 400°C. This maximum temperature needed to produce α-SnS was significantly lower than results reported by Sousa et al.[19] but the annealing times used here were much longer. Choice of heater had a significant impact on formation of the α-SnS phase due to the rate of cooling. The fast cooling associated with the halogen heater caused samples annealed under the same parameters to yield different results. The morphology seen in the SEM suggests a time line of what occurs during the annealing process for samples grown at room temperature: (1) Sample C1 shows that amorphous tin sulfide converts to small crystallites of Sn_2S_3 forming early in the anneal; (2) Sample D3 shows the intermediate step of these crystallites reforming into larger grains; (3) Samples C2 and C3 show a final stage of annealing in which large grains have formed. Based on the progression of the morphology, it is likely that a 40–50 min anneal at 400°C using the halogen lamp may yield a film more similar to sample D3.

CONCLUSIONS

Formation of α-SnS thin films via annealing of sputtered tin sulfide from a SnS_2 target was achieved. Depositing from the SnS_2 target at room temperature produced amorphous films, enabling crystallization into Sn_2S_3 or α-SnS during annealing, dependent on time and temperature. α-SnS films produced via these methods had significantly better electronic properties than films made from a SnS target.[14,17] The morphology of the films showed large crystallites and resistivity values < 100 Ω-cm, and suggests that this method of processing will be better for integrating these films into photovoltaic devices. Phase formation matches well to phase diagrams calculated for low-pressure systems. Annealing to form α-SnS from as-deposited films is possible with vacuum anneals at 400°C with sufficient time. Increasing the temperature and decreasing the annealing time could yield α-SnS, but this must be done at increased pressure to ensure better control of the process. Regardless of the phase present in thin films, reaction progress tends to the vaporization of sulfur and reduction of tin for annealing in the vacuum environment. A faster annealing process would be better for PV device processing. Based on the calculations, annealing in the temperature range of 395–430°C is suggested for pressures around 1×10^{-4} Pa. While sulfur-deficient films can have large defect concentrations due to low formation energy of tin vacancies, these calculations showed that annealing in sulfur atmosphere is likely to yield unwanted secondary phases. Utilization of these types of phase diagram calculations will accelerate identifying the best process for future development of this material, particularly when as-grown doping of the material is investigated.

ACKNOWLEDGEMENTS

The authors would like to acknowledge the assistance of the Materials Characterization Lab staff and the facilities at Penn State University. Additional thanks are extended to Drs. T. Jackson and S. Mohney and their students for allowing us to use their facilities for Ti depositions and electronic measurements. This work was partly financially supported by NSF with Grant Nos. CHE-1230924.

REFERENCES

1. L.A. Burton and A. Walsh, *Appl. Phys. Lett.* 102, 13 (2013).
2. T. Sorgenfrei, F. Hofherr, T. Jauss, and A. Croll, *Cryst. Res. Technol.* 48, 4 (2013).
3. M. Devika, N.K. Reddy, K. Ramesh, R. Ganesan, K.R. Gunasekhar, E.S.R. Gopal, and K.T.R. Reddy, *J. Electrochem. Soc.* 154, H67 (2007).
4. K.T.R. Reddy, N.K. Reddy, and R.W. Miles, *Sol. Energy Mater. Sol.* 90, 18 (2006).
5. J.L. Loferski, *J. Appl. Phys.* 27, 7 (1956).
6. P. Sinsermsuksakul, L. Sun, S.W. Lee, H.H. Park, S.B. Kim, C. Yang, and R.G. Gordon, *Adv. Eng. Mater.* 4, 15 (2014).
7. H. Noguchi, A. Setiyadi, H. Tanamura, T. Nagatomo, and O. Omoto, *Sol. Energy Mater. Sol. C* 35, 1 (1994).
8. S.S. Hedge, A.G. Kunjomana, K.A. Chandrasekharan, K. Ramesh, and M. Prashantha, *Physica B* 406, 5 (2011).
9. P. Sinsermsuksakul, J. Heo, W. Noh, A.S. Hock, and R.G. Gordon, *Adv. Eng. Mater.* 1, 6 (2011).
10. L.A. Burton, D. Colombara, R.D. Abellon, F.C. Grozema, L.M. Peter, T.J. Savenije, G. Dennler, and A. Walsh, *Chem. Mater.* 25, 24 (2013).
11. N. Reddy and K.T.R. Reddy, *Mater. Chem. Phys.* 102, 1 (2007).
12. M. Devika, N.K. Reddy, D.S. Reddy, Q. Ahsanulhaq, K. Ramesh, E.S.R. Gopal, K.R. Gunasekhar, and Y.B. Hahn, *J. Electrochem. Soc.* 155, H130 (2008).
13. S. Cheng, G. Chen, Y. Chen, and C. Huang, *Opt. Mater.* 29, 4 (2006).
14. R.E. Banai, H. Lee, M.A. Motyka, R. Chandrasekharan, N.J. Podraza, J.R.S. Brownson, and M.W. Horn, *IEEE J. Photovolt.* 3, 3 (2013).
15. K. Hartman, J.L. Johnson, M.I. Bertoni, D. Recht, M. Aziz, M.A. Scarpulla, and T. Buonassisi, *Thin Solid Films* 519, 21 (2010).
16. J.R.S. Brownson, C. Georges, and C. Levy-Clement, *Chem. Mater.* 18, 26 (2006).
17. R.E. Banai, H. Lee, S. Zlotnikov, J.R.S. Brownson, and M.W. Horn, *IEEE Photovoltaic Specialists Conference*, 2013.

18. R.E. Banai, H. Lee, M. Lewinsohn, M.A. Motyka, R. Chandrasakharan, N.J. Podraza, J.R.S. Brownson, and M.W. Horn, *IEEE Photovoltaic Specialists Conference*, 2012.
19. M.G. Sousa, A.F. da Cunha, and P.A. Fernandes, *J. Alloys Compd.* 592, 80 (2014).
20. R.C. Sharma and Y.A. Chang, *Bull. Alloy Phase Diagr.* 7, 3 (1986).
21. L. Kaufman and H. Bernstein, *Computer Calculation of Phase Diagrams* (New York: Academic Press, 1970).
22. N. Saunders and A.P. Miodownik, *CALPHAD (Calculation of Phase Diagrams): A Comprehensive Guide*, ed. R.W. Cahn (Oxford: Pergamon, 1998).
23. Z.K. Liu, *J. Phase Equilib. Diff.* 30, 5 (2009).
24. Z.K. Liu, D.G. Schlom, W. Li, and X.X. Xi, *Appl. Phys. Lett.* 78, 23 (2001).
25. J.F. Ihlefeld, N.J. Podraza, Z.K. Liu, R.C. Rai, X. Xu, T. Heeg, Y.B. Chen, J. Li, R.W. Collins, J.L. Musfeldt, X.Q. Pan, J. Schubert, R. Ramesh, and D.G. Schlom, *Appl. Phys. Lett.* 92, 14 (2008).
26. B. Van Zeghbroeck, The "hot-probe" experiment (2011), http://ecee.colorado.edu/~bart/book/book. Accessed 7 July 2015.
27. V. Piacente, S. Foglia, and P. Scardala, *J. Alloys Compd.* 177, 1 (1991).